Ultra-high-resolution monolithic thermal bubble inkjet print head

Yan Wang
Xilinx Incorporated
2100 Logic Drive
San Jose, California 95124
E-mail: yanw@xilinx.com

Jeffrey Bokor
University of California at Berkeley
Electrical Engineering and Computer Sciences
    Department
508 Cory Hall
Berkeley, California 94720

Abstract. A monolithic inkjet print head, fabricated with silicon micromachining technology and capable of generating microscale liquid droplets, is developed and shown to function successfully. The print head uses a dense array of thermal bubble inkjet devices, made on a single silicon wafer. Each device is made of a Pt heater stack, a small, shallow fluid chamber, and a refilling channel formed by a Ge-sacrificial etching process, a deep-etched through-wafer feeding hole, and a micron-scale nozzle opened in a thin nitride membrane by plasma etching. Experimental results with a high resolution video imaging system show that this print head is capable of generating water droplets as small as 3 μm in diameter (0.014 pL), about 1/70th the volume of the droplets produced by existing inkjet systems. The printing process is also found to be stable, uniform in droplet size and velocity, and free of satellite droplets at optimum operation conditions. At small distances between the print head and substrate, droplet spreading is also small. This print head is then a capable tool for ultra-high-resolution inkjet printing and can be used in research areas where delivery of micron-scale fluid droplets is desired. © *2007 Society of Photo-Optical Instrumentation Engineers.* [DOI: 10.1117/1.2816449]

1 Introduction

The drop-on-demand (DOD) inkjet device, which expels a small fluid droplet on application of an electronic signal, has been widely used in the commercial inkjet printing industry for it low cost and color capability.[1,2] The state of the art inkjet cartridges have thousands of nozzles, and typically deliver liquid droplets with volume larger than 1 pL,[3,4] which could create ink spots larger than 15 μm in diameter on a piece of paper.

Recent years have also seen a growing interest in applying inkjet printing technology into micro/nano research areas. DOD inkjet devices have been widely used for molecule detection,[5] protein and DNA synthesis,[6] nanoparticle deposition,[7] as well as direct writing of organic transistor circuits,[8] and microelectromechanical system (MEMS) devices.[9] For these applications, the minimum printable droplet dimension is a critical parameter influencing the accuracy of analysis and deposited feature resolution. Consequently, there is strong motivation to develop inkjet print heads that have micron to submicron scale resolution, high droplet delivery speed, and also good chemical compatibility.

A variety of actuation mechanisms have been reported for DOD inkjet devices, including piezoelectric,[10,11] thermal bubble,[12–18] acoustic,[19] and electrostatic.[20] Among them, the piezoelectric and thermal bubble devices are most mature and commonly used in inkjet printers. Although commercially successful today, the piezo-based print heads use a bulk piezoelectric material as the pressure transducer, which requires a large device area to achieve enough actuation strength and displacement volume; the number of inkjet devices on a print head is thus limited. The acoustic and electrostatic devices also need a large transducer area for performance concerns. The thermal bubble inkjet devices, on the other hand, utilize growth of a vapor bubble on a heater surface for actuation. They are smaller, more easily fabricated, and have no moving mechanical parts. They are therefore more robust, and hence an ideal device for a compact print head with large array of DOD devices for high-resolution, high-speed printing. A comparison of the typical actuator size for different types of DOD inkjet devices is shown in Table 1.

Existing thermal bubble inkjet print heads, however, lack the capability to produce sub-10-μm-diam droplets, mostly due to their design and fabrication process. Commercial thermal bubble inkjet cartridges are made by bonding two or more pieces together to form a final structure.[12,13] The nozzle and chamber resolution is limited by the accuracy of alignment. Some groups have reported monolithic thermal bubble print heads made without the bonding process. Their print heads, however, either have limited nozzle radii,[15,16] large chamber dimensions,[14] or thick nozzle membranes,[17] which are all disadvantageous in reducing the droplet size. As shown in Table 2, the smallest droplet size that is reported for a thermal bubble inkjet device is around 0.9 pL.

In this work, we present the design and fabrication process of a monolithic thermal bubble inkjet print head based on silicon micromachining technology. The print head has

Table 1 Comparison of inkjet device actuator size with different actuation mechanisms.

Reference device	Type	Actuator size	Device/Head
Epson Stvlus 800[1]	Piezoelectric	$>140 \times 500$ μm	180
HP/Canon[4,12]	Thermal bubble	$<30 \times 30$ μm	>1000
Huang and Kim et al.[19]	Acoustic	400×400 μm	NA
Kamisuki et al.[20]	Electrostatic	367 μm	>1000

precisely defined inkjet nozzles, chambers, and actuators, formed on a single silicon wafer for micron-scale droplet generation. Test results with a high resolution video imaging system show that this print head has excellent performance in droplet resolution (down to 3-μm droplet size realized) and quality (uniform droplet size, without formation of satellite droplets).

2 Printhead Design

2.1 Device Mechanism and Simulation Result

In a thermal bubble inkjet device, a smooth, microfabricated heater heats a thin layer of liquid to its superheated temperature limit ($\sim 300\,^{\circ}$C for water) in several microseconds.[21] Homogeneous nucleation occurs at the liquid-solid interface, and the liquid evaporates explosively into the nucleus, forming a high-pressure vapor bubble. The expansion of the bubble drives the fluid inside an inkjet chamber, pushing a liquid column through a nozzle. As the energy is removed from the superheated liquid layer by evaporation, both the bubble temperature and pressure decrease. The bubble collapses when its pressure falls below the ambient pressure, and draws the fluid at the nozzle backward, forming a thin neck. The liquid head detaches if the neck is sufficiently small. The detached fluid forms a spherical shape under surface tension. At the same time, the chamber is refilled by capillary force for the next operation cycle. The whole operation cycle is illustrated in Fig. 1.

To design a thermal bubble inkjet print head capable of generating droplets smaller than that of the existing inkjet printing systems, we have studied the droplet formation process using a commercial inkjet simulation tool—CoventorWare$^{\text{TM}}$ (Conventor, Cary, North Carolina).[22] The core of the software is a Flow-3D engine, which utilizes a volume of fluid (VOF) method to treat the liquid-gas inter-face deformation during bubble formation and droplet break-up. In our simulation, a pressure pulse is applied to a fluid chamber with a small nozzle on top (gravity is negligible in a micron scale). We found that the printed droplet dimension is typically comparable or larger than the nozzle size. To reduce droplet size, a smaller nozzle is a must. However, as nozzle size decreases, the pressure magnitude needs to be increased to overcome the increased surface tension and viscous force that opposes droplet ejection. The nozzle shape itself also has a big impact on droplet formation. A thinner nozzle will have smaller flow resistance; therefore a lower actuation pressure is needed for droplet ejection.

Following the work of Asai,[23] we used a simple equation to approximate the fluidic pressure P_b generated by a thermal bubble inkjet device:

$$P_b = (P_g - P_s)\exp[-(t/t_o)^{1/2}] + P_s. \tag{1}$$

P_g is equal to the saturated vapor pressure of the fluid at the nucleation temperature, which is fixed to be around 4 MPa for water.[24] P_s is the saturated vapor pressure at room temperature (~ 27 kPa), and t_o is a time constant characterizing the total "strength" of the bubble actuation; this parameter is determined by the inkjet design. It can be easily understood that the more energy available for vapor evaporation and the higher the total fluidic resistance to bubble expansion, the bigger t_o will be. Applying this simple pressure profile to a nozzle with fixed aspect ratio of 2:1, we found that the minimum printable water droplet size (droplet detaches with velocity larger than 1m/s) is about 0.5 μm through a 0.4-μm nozzle. The simulated droplet formation

Table 2 Compact thermal bubble inkjet print head with droplet size smaller than 20 μm.

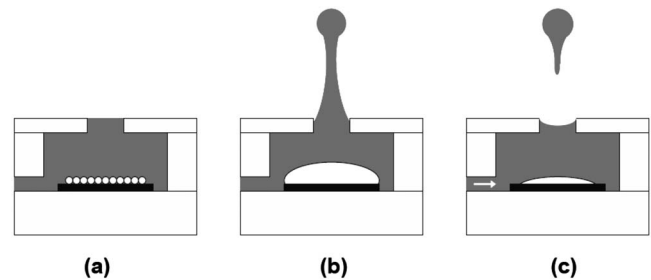| Reference device	Type	Diameter (volume)	Device/ Head
HP Desk Jet 9800	Thermal	18 μm (3 pL)	1280
Canon IP5200[4]	Thermal	12.5 μm (1 pL)	3584
Tseng, Kim, and Ho[17]	Thermal	12 μm (0.9 pL)	Array
Chen and Wise[15]	Thermal	20 μm (4 pL)	16

(a) **(b)** **(c)**

Fig. 1 The operation cycle of a thermal bubble inkjet device: (a) nucleation occurs on the heater surface when the liquid temperature reaches a superheated temperature limit; (b) bubble growth and liquid column ejected from inkjet nozzle; and (c) bubble collapses and droplet breaks up from nozzle, at the same time chamber is refilled by capillary force.
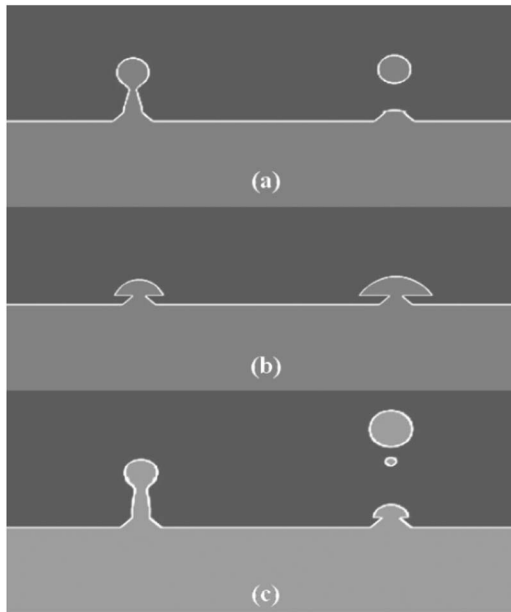
Fig. 2 Simulated droplet formation sequence for thermal bubble ink-jet device: (a) a 0.5-μm scale droplet generation through a 0.4-μm nozzle with t_o=0.1 μs; (b) no droplet formation for a 0.2-μm nozzle with t_o=0.2 μs; and (c) satellite droplet generated for 1-μm nozzle with t_o=0.05 μs.

Fig. 3 (a) The perspective view of our monolithic thermal bubble inkjet print head with array of inkjet devices. (b) Cross section view of a single inkjet device.

sequence is shown in Fig. 2(a). With an even smaller nozzle, only a fluid meniscus will be formed outside the nozzle and no droplet breakup will occur no matter how large the t_o is [Fig. 2(b)]. Not surprisingly, we also found that the required t_o value for single droplet formation increases as the nozzle size decreases. It is about 0.02 μs for a 10-μm nozzle in our simulation, and 0.1 μs for the 400-nm nozzle. With the same nozzle dimension, a larger t_o would result in a droplet with higher speed, or finally satellite droplet formation as shown in Fig. 2(c).

The actual bubble pressure of a thermal bubble inkjet device can be much more complicated than the simple exponential shape used in our simulation. However, the simulation results still give us good indication that micron and even submicron scale droplet generation is possible with a thermal bubble inkjet device. Decreasing the nozzle size, increasing the chamber pressure generated by the bubble actuation, as well as reducing fluid resistance to droplet ejection, are the keys to a high-resolution inkjet print head design.

2.2 Print Head Design

Figure 3(a) shows the schematic structure of a monolithic thermal bubble inkjet print head designed for high-resolution, high-speed printing applications. The print head composes a dense array of thermal bubble inkjet devices made on top of a silicon substrate with integrated controlling circuits. The cross section view of a single device is illustrated in Fig. 3(b). A "top-shooter" structure is implemented, where an inkjet nozzle is opened on a membrane directly on top of a thin film heater, separated by a shallow fluid chamber. Consequently, the nozzle radius becomes independent with other inkjet dimensions and can be reduced to microscale using micromachining technology. The inkjet
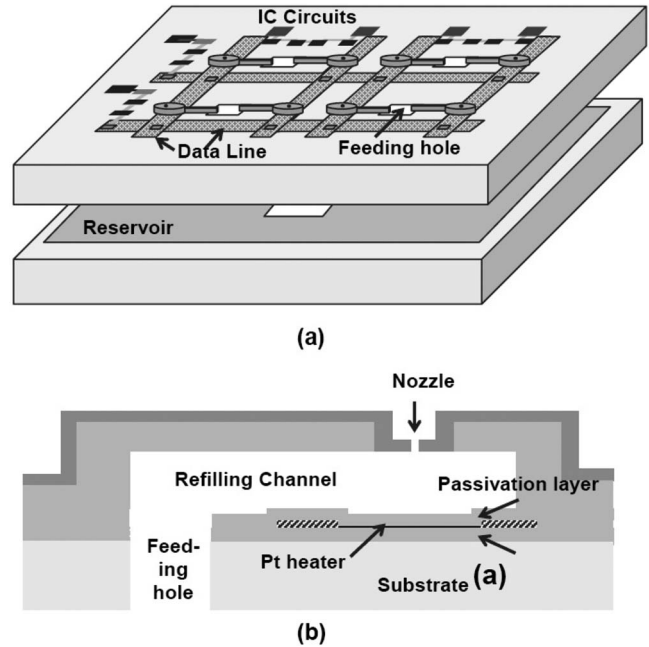
chamber is connected to a liquid reservoir on the back side of a silicon substrate by a through-wafer feeding hole and a small refilling channel. The fluid refilling system is designed so that its flow resistance is slightly higher than that of the inkjet nozzle;[25] as a result, little liquid will flow back into the reservoir as bubble grows. The bubble actuation efficiency is increased and cross talk between adjacent inkjet devices is minimized. At the same time, the chamber refilling time is still sufficiently small for high inkjet operation frequency. In our print head, refilling channels with length of about 100 μm and cross section of 10×20 μm, and feeding holes around 100 μm (through 500-μm-thick substrate), are used for the micron scale nozzles.

Small, shallow fluid chambers are designed for our inkjet device. A shallow chamber reduces the acoustic loss of the pressure wave generated by bubble expansion, while a small chamber area can help to increase the device density on the substrate, while decreasing the fluid damping and refilling time. Using a Ge-sacrificial etching process (refer to the next section), inkjet chambers with depth around 5 μm and size ranging from 60 to 100 μm (depending on heater dimension) are formed on our print head.

As discussed in the previous section, a thinner nozzle will have smaller flow resistance, hence a smaller droplet can be generated with the same actuation condition. Reducing the nozzle membrane thickness is then an effective approach to improve droplet resolution. However, a thinner membrane is also less robust. Since the whole inner surface of the inkjet chamber is subjected to the actuation pressure, flexing of the nozzle membrane would reduce the fluid pressure across the nozzle. For this reason, the top membrane of our device is separated in two parts, a thin and small nozzle plate and a thick surrounding ceiling structure [Fig. 3(b)]. Since the membrane rigidity scales inversely to
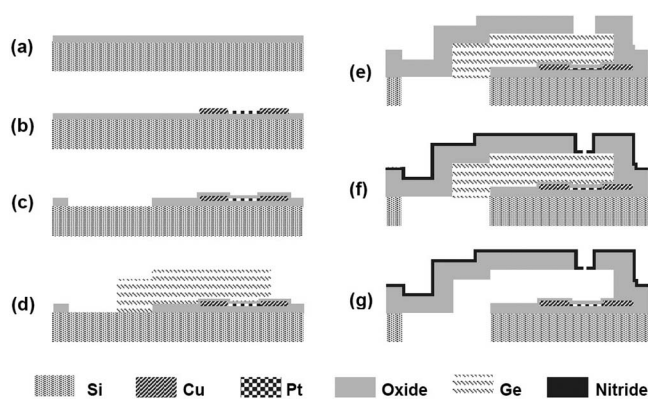
Fig. 4 Process flow for monolithic thermal bubble inkjet print head fabrication.

the fourth power of its radius and the third power of its thickness, the membrane as a whole is strong enough to sustain the high pressure for small droplet ejection.

Square-shaped thin film Pt resistors are used as the heating element in our device because of their excellent thermal stability. A heater is sandwiched between a passivation layer and a heat barrier [Fig. 3(b)]. The passivation layer, which is made of 0.7-μm chemical vapor deposited (CVD) silicon dioxide, works both for electrical insulation and the protection of the heater surface from the rough cavitation force of collapsing bubbles. A thinner layer would be more thermally efficient, but less mechanically resilient.[26] A 2.0-μm oxide layer is used as the heat barrier to prevent excessive heat loss from the heater to the silicon substrate. Its thickness was optimized by performing a 1-D thermal diffusion simulation of heater operation, and balancing between the energy consumption and system cooling time. The heater size and the heating electrical signal profile will significantly influence the energy transferred into the liquid for bubble evaporation, hence the pressure available for droplet formation as discussed in the previous section. However, due to the complicated nature of thermodynamic and hydrodynamic coupling between the heater, the vapor bubble, and the liquid system, no direct model can predict the appropriate heater size and driving condition for micron-scale droplet generation with certainty. These parameters will then be optimized experimentally.

3 Print Head Fabrication

3.1 Fabrication Process

The process flow to fabricate the proposed print head is shown in Fig. 4. It begins with a deposition of 2.0-μm low-pressure chemical vapor deposition (LPCVD) silicon dioxide on a 4-in. silicon wafer as the heat barrier [see Fig. 4(a)]. Ti/Pt/Ti heaters with thickness of 10/40/10 nm and sheet resistance of 14 $\Omega/\square$ are formed by magnetron sputter deposition and photoresist lift-off patterning. Another lift-off and electron-beam evaporation process is used to form the Cu interconnect lines [see Fig. 4(b)]. After deposition of 0.7-μm LPCVD oxide as the passivation layer, the oxide is etched from the area where the liquid feeding holes will be formed with buffered HF acid [see Fig. 4(c)]. It is followed by a 10-nm Si seed layer growth and a 10-μm LPCVD poly-Ge deposition. The rough Ge surface is flat-

tened by a chemical mechanical polishing (CMP) process and patterned by plasma etching (with Cl/HBr gas) to form the dummy structures of liquid chambers and refilling channels [see Fig. 4(d)]. Deposition of 6-μm CVD oxide encapsulates the Ge dummy structures; the film is then wet etched to open the small area where the nozzle plates will be formed [see Fig. 4(e)]. Plasma-enhanced chemical vapor deposition (PECVD) at 300°C deposits a 1-μm low stress silicon nitride layer as the nozzle plate film.

Liquid feeding holes with size of 100 μm are patterned on the back of the wafer and etched through it by the deep reactive ion etching (DRIE) process. The etching stops at the thick oxide layer and Ge dummy in the front [see Fig. 4(f)]. Ge is then removed from the refilling channels and inkjet chambers through the feeding holes with 150°C hot H_2O_2. The whole process typically takes several hours. After the sacrificial structures are removed, the Cu bonding pads are exposed, and micron-scale nozzles are patterned on the thin nitride membranes by plasma etching [see Fig. 4(g)]. The nozzle region is then coated with 100-nm Ti/Ni as an antiwetting layer by electron-beam evaporation. The antiwetting coating is to prevent the formation of a liquid meniscus, which would interact with the droplet column and reduce droplet generation stability.

Test chips of the print head have been successfully fabricated using the previous process. Figure 5(a) shows an optical micrograph of a wire bonded chip with antiwetting coating at the nozzle region. The chip has an array of inkjet devices with varying heater (50 to 20 μm) and chamber dimensions [Fig. 5(b)]. A close-up view of an inkjet chamber (without the Ni coating) is illustrated in Fig. 5(c). The chamber diameter is 60 μm, with a wall and top ceiling thickness of 7 μm, while the nozzle plate is 1 μm thick and about 8 μm in radius. A square-shaped heater can be seen beneath the transparent top membrane. The smallest nozzle size that can be fabricated by plasma etching is about 2.5 μm, determined by the lithography resolution of the front/back exposure tool used in our process. A scanning electron microscope (SEM) picture of a 3-μm nozzle with a perfect round shape is shown in Fig. 5(d). To investigate the limit of droplet size that can be generated from our print head, test chips with nozzle diameter between 1.1 and 2 μm are also fabricated using the focused ion beam drilling method. A SEM picture of a 1.1-μm nozzle drilled through the top nitride membrane of an inkjet device is shown in Fig. 6.

3.2 Advantages of Our Print Head Fabrication Process

Compared with previously reported inkjet head fabrication methods, our print head fabrication process has the following advantages.

1. The print head is fabricated on a single silicon wafer without a bonding process, reducing fabrication complexity and increasing the device yield.
2. The process accuracy is only limited by the optical lithography resolution and is in the micron range; our inkjet design could be fully implemented to print microscale droplets.
3. The inkjet chambers and nozzles are made of chemically compatible materials such as silicon, silicon di-
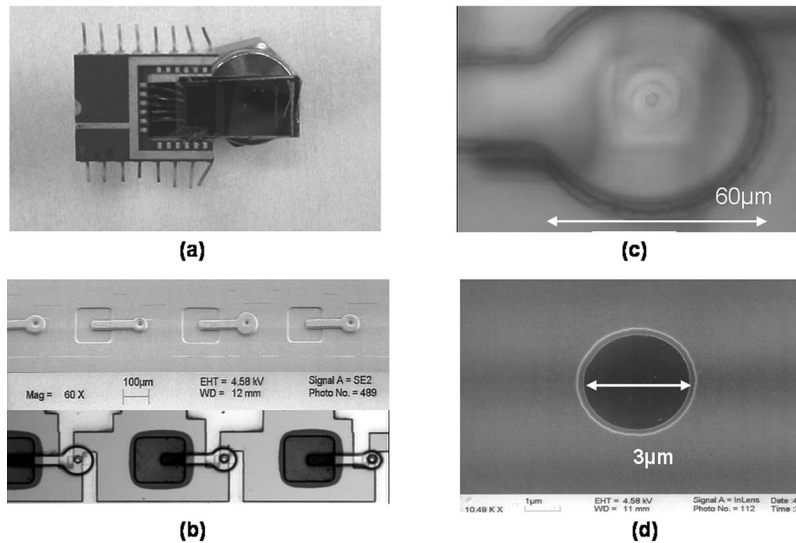
Fig. 5 (a) Wire bonded test chip with fluidic connection and antiwetting coating. (b) Array of inkjet chambers and refilling channels. (c) Top view of a single inkjet device with 5-μm nozzle. (d) SEM picture of a 3-μm nozzle.

oxide, and silicon nitride. The print head can then be used to print a variety of materials.

4. The inkjet devices are small enough (smaller than 80×200 μm with 50-μm feeding holes) to allow a large, densely packed array of inkjet devices to provide a high printing throughput.

5. The inkjet structure is robust, with thick chamber walls and small nozzle membranes, for a long operational lifetime.

6. The inkjet print head is fabricated by a monolithic process, so switching circuits can be integrated with the inkjet devices to increase data transfer and handling rate.

4 Experimental System

4.1 Video Imaging System

To discover the minimum producible droplet size of our inkjet print head and find optimum operation conditions for stable, satellite-drop-free droplet formation, we have constructed a video imaging system to capture the sequence of droplet generation from the test chips. The block diagram of our experimental setup is shown in Fig. 7. Several pulse generators are synchronized to provide square-shaped elec-
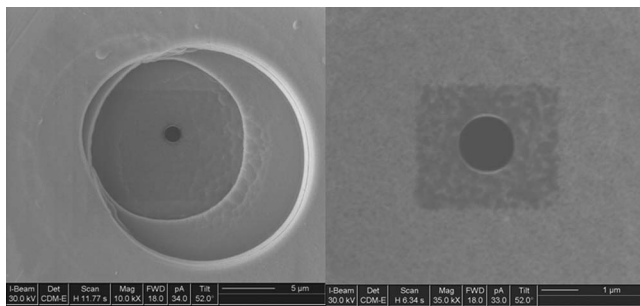

Fig. 6 SEM picture of a 1.1-μm nozzle fabricated by focused ion beam drilling.

tric pulses with adjustable magnitude and width to drive the heaters and trigger a strobe light source. A $100\times$ long-working-distance Mitsubishi objective lens is mounted with an externally triggered black and white charge-coupled device (CCD) camera. The camera and strobe light are both focused at the nozzle, providing a resolution of about 1 μm. A TV monitor and a digital video recorder receive the camera's output and convert the analog video signal to digital, recording it on mini DV tapes. A computer with video capturing and editing software is used to capture the desired frames in the videos.

4.2 Preparation of the Test Chips

The test chip is prepared for experiments by bonding it to a handling chip with chemically resistant epoxy. The handling chip has a 100-μm-deep cavity in the front, opened to all the inkjet chambers, and a hole at the back. Through this hole, the chip pair is connected to a fluidic delivery system, as illustrated in Fig. 3(a). The test chip is then mounted inside a vacuum chamber to evacuate all air from the chip. A valve is then opened and liquid fills all the mirochannels in the chip under atmospheric pressure. The vacuum chamber is then vented, and excessive liquid outside the nozzles is absorbed by lens paper. The liquid-filled chip is carefully mounted on an *xyz* stage. Height differences between the liquid reservoir and the inkjet nozzles are balanced to maintain a small positive background pressure without leaking of the liquid from the nozzles.

5 Experimental Results

5.1 Droplet Generation

We have tested our inkjet devices using deionized water that has been filtered to be free of particles. Stable, single-droplet generation has been observed by adjusting the heating electrical signal (discussed in the next section). The observed minimum droplet size versus nozzle diameter is listed in Table 3. The droplet size is measured by comparison to a reference length mark patterned on the test chip
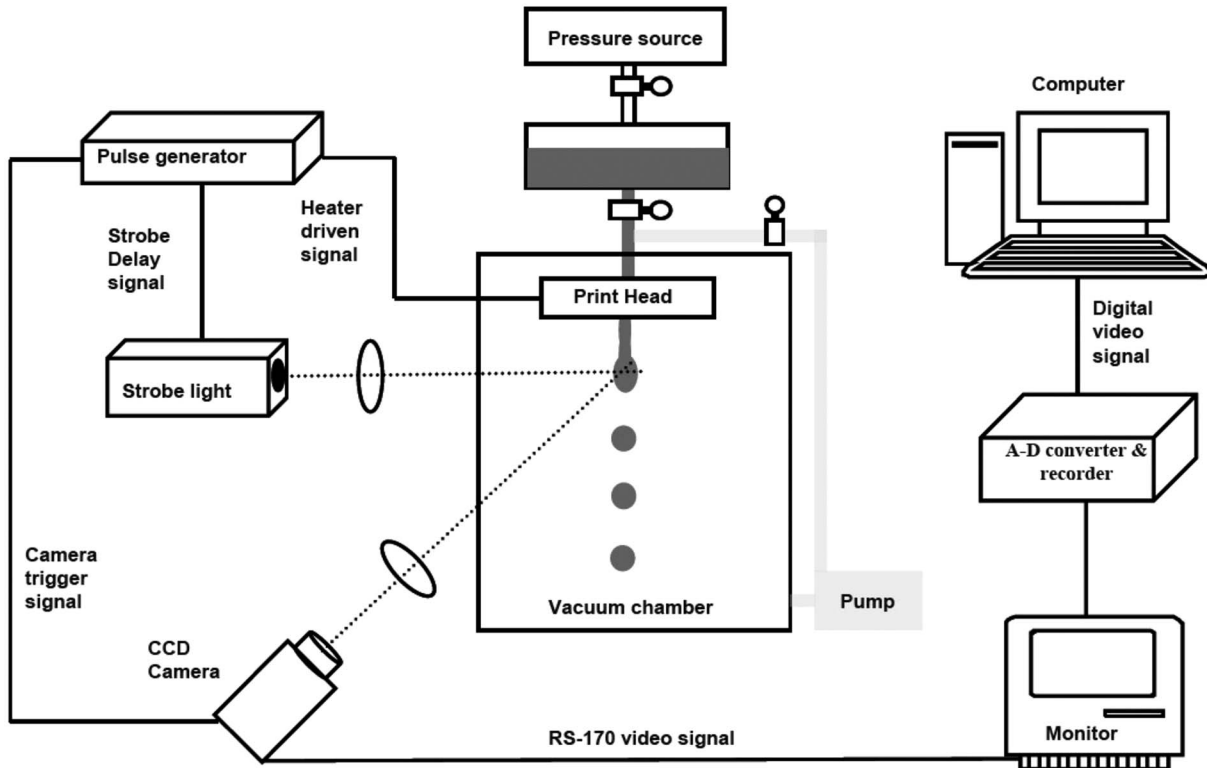
Fig. 7 Experimental setup with video imaging and fluid delivery system.

surface. For nozzle size in the 7– to 2 μm range, the droplet size is directly proportional to the nozzle dimension. However, as the nozzle size is decreased below 2 μm (the FIB drilled nozzles), the ejected droplet diameter is almost fixed around 3 μm. Further reducing the nozzle size could not effectively reduce the droplet size, contrary to our numerical simulation result. The discrepancy could come from a much more complicated bubble pressure profile in a real inkjet device. The 3-μm droplet size is already one-fourth the size of that produced by the most advanced inkjet cartridges, and is the smallest that has ever been reported for a compact inkjet print head.

The droplet formation sequence of a 10-μm droplet generated from a 7-μm nozzle is shown Fig. 8. A liquid column can be seen formed outside the nozzle, and a thin neck evolves before droplet detachment. The total droplet formation time (from emergence of liquid head to break-up) is around 5 μs. The tail beneath the droplet is due to the finite pulse width of our strobe light and the droplet motion during the strobe flash. Figure 9 shows a single 3-μm droplet generated from a 1.5-μm nozzle; the droplet formation

time is around 1.5 μs, much shorter than the 10-μm scale droplet, which is consistent to our numerical simulation result.

5.2 *Influence of Heating Signal and Heater Size*

As predicted by the thermal bubble inkjet theory, the droplet formation process strongly depends on the input heating signal. However, the behavior is quite different with different nozzle dimensions. For a relatively big nozzle (4 to 7-μm scale), if the heating time is fixed (typically several microseconds), droplet ejection happens once the input heating voltage reaches the bubble formation condition (the fluid temperature at the heater surface exceeds the nucleation temperature). Increasing the electric pulse magnitude can quickly increase the ejected droplet velocity and cause

Table 3 Typical droplet size versus nozzle diameter.

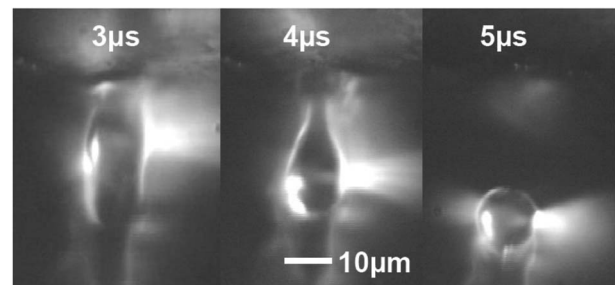| Nozzle size (μm)	7	5	3.5	2.5	2	1.5	1.2
Droplet size (μm)	10	7	5	3.5	~3	~3	~3

Fig. 8 Single droplet formation sequence from a 7 μm nozzle with 8 V/4 μs heating signal. The droplet size is about 10 μm; the total droplet formation time is 5 μs.

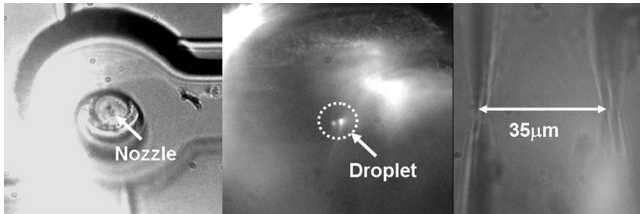**Fig. 9** A 3-μm single water droplet generated from a 1.5-μm nozzle. Left: nozzle view; middle: 3-μm droplet; right: the reference length mark.

satellite droplet formation, as shown in Fig. 10. If a longer heating pulse is used, the initial droplet formation voltage decreases; however, the ejected droplet velocity increases. This phenomenon can be explained by a lower thermal flux resulting in a thicker superheated liquid layer, allowing more energy for vapor evaporation, hence causing higher bubble actuation strength. There is a limit to the driving voltage for given pulse width; above this, the heater will overheat and break down.

If the nozzle size is smaller than 3 μm, however, no droplet breakup is observed immediately after the heating signal exceeds the bubble formation condition. A liquid head forms outside the nozzle, but it retracts back to the chamber as the bubble collapses (the liquid head dimension is too small to be distinguished in a picture, but can be clearly seen in a video frame). A single droplet ejects only when the input heating voltage and pulse width reaches a certain level. When a droplet barely forms, its velocity is quite small. Increasing the driving voltage and pulse width would increase the droplet velocity and enlarge the droplet size slightly. But no satellite droplet is observed until an extremely long heating pulse is used.

The initial droplet generation and heater breakdown conditions for an inkjet device with a 7-μm nozzle and 30-μm heater (total heater resistance is 26 Ω) are plotted in Fig. 11. The shadowed area indicates the single droplet formation region. Similar operation windows are also plotted for a 2.5-μm nozzle and a 1.5-μm nozzle, respectively (the nozzle thicknesses are both 1 μm). We can see that the window is shifted to the right as the nozzle size decreases, indicating that more heating energy, hence stronger bubble actuation strength, is necessary for a smaller droplet ejection. The window size also becomes larger; hence satellite
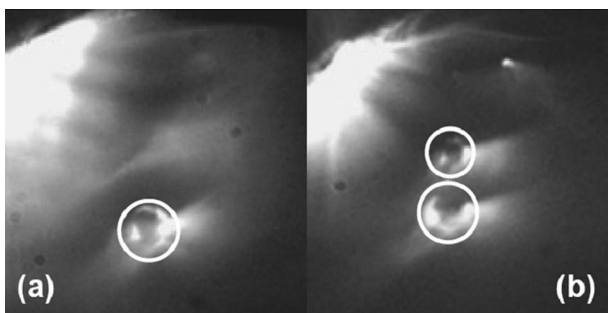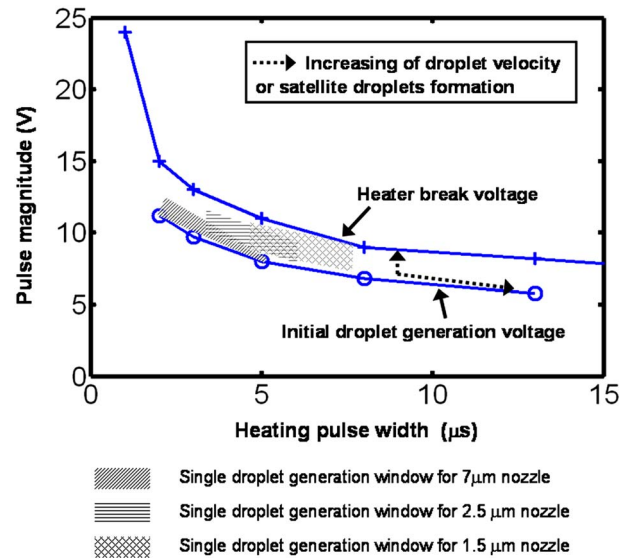

Fig. 11 Droplet generation and heater break-down conditions for inkjet devices with 2.5-μm nozzles and 30-μm heaters. The shadowed area is the optimum operation window for this kind of device.

free droplet formation can be more easily achieved for the smaller nozzles. The maximum velocity we have observed for the 3-μm scale droplets in the single droplet formation window is about 15 m/s.

Heater sizes ranging from 50 to 20 μm have been fabricated in our test chips. Larger heaters tend to form droplets with bigger volume and velocity at the same driving pulse width and thermal flux (power/area) according to our experimental result, which is reasonable, considering more energy is transferred to the superheated liquid layer. However, their influence on droplet generation can be easily overpowered by slight changes in the heating signal. The heater size effect only becomes dominant when the heater dimension is reduced to 20 μm. At this heater size, no droplet detachment has been observed for 1.5-μm nozzles under any driving condition.

5.3 Droplet Uniformity and Trajectory Spreading

The challenge of high-resolution printing does not end with reducing droplet size; consistent droplet volume and accurate positioning on the substrate are also essential. Experimental results show that droplets produced by our print heads are extremely uniform. Once the driving condition is fixed, the droplet generation process is stable, and the observed longitudinal droplet velocity distribution is smaller than 5%, while droplet size change is not detectable [refer to Figs. 12(a) and 12(b)].

The droplets will travel in a straight line after detaching from the nozzle, gradually losing their momentum to air resistance, since the system is operated in atmosphere. The misplacement of a droplet on a substrate can be attributed to two factors: the original droplet's angular velocity distribution and the random movement of the droplet due to air molecule collisions. We have captured droplet trajectory distributions of the 3.5-μm droplets generated from our print head at different flight distances by setting different delay times to the strobe trigger signal. As shown in Fig.
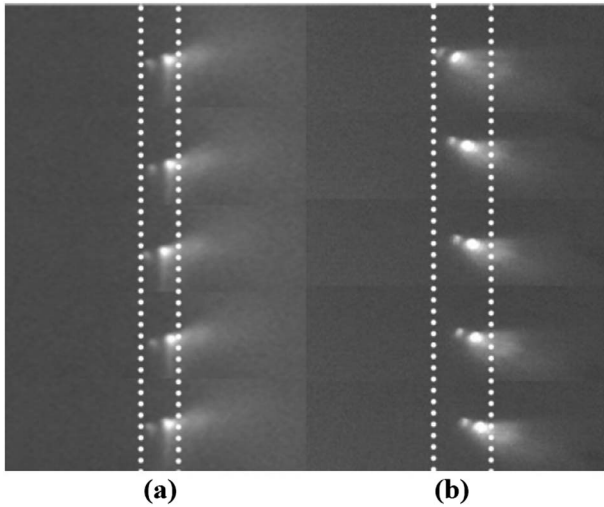

Fig. 10 Influence of driving electric signal on droplet generation with a 5-μm nozzle and 30 μm heater: (a) single droplet formed at 8.5 V/4 us; and (b) satellite droplet formed at 7 V/10 μs.

Fig. 12 (a) Droplet trajectory distribution at delay time of 50 μs, flight distance around 150 μm, and velocity about 2 m/s. (b) Droplet trajectory distribution at delay time of 300 μs, distance about 300 μm; and droplet velocity is almost zero.

12(a), when the droplet flight distance is short and the droplet velocity is high, the droplet trajectory spread, mostly due to the original droplet angular velocity distribution, is much smaller than the droplet size. When the strobe delay time is further increased to 300 μs, as shown in Fig. 12(b), the droplet has traveled about 300 μm and its velocity is almost zero. The droplet spread increases dramatically because of Brownian motion.

The observed stopping distances and flight times of different droplet sizes and original velocities are listed in Table 4. The droplet flight distance is almost proportional to the square of droplet size and first power of velocity, which is consistent with theoretical calculations, assuming that the droplet is slowed by air drag force. The working distance between our print head and the substrate should then be kept smaller than this distance to achieve high printing quality. Flight distance could be greatly increased by operating the system in a low-pressure environment, which would extend the droplet mean free path.

5.4 Throughput Analysis

Many applications of DOD inkjet systems, especially the printing of paper documents, require that the print head deliver liquid droplets with high speed. We could not directly observe the print head performance at frequencies higher than 150 Hz, due to the limitations of our experi-

Table 4 Microdroplet stopping distance and flying time.

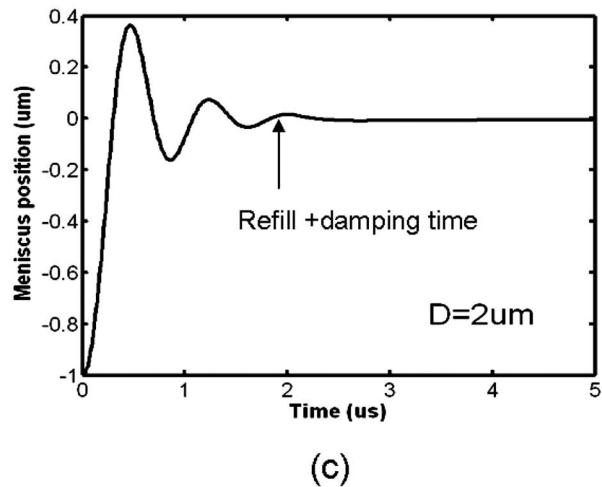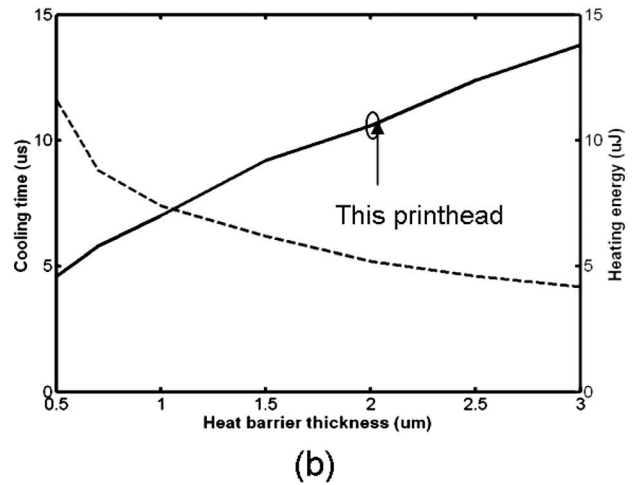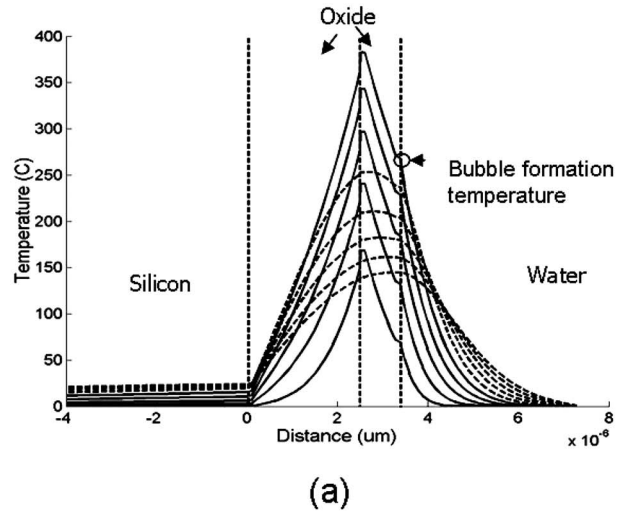| Droplet size (μm)	7	7	3.5	3.5
Velocity (μm)	5	3	5	3
Stopping distance	1100	700	300	200
Flying time (μm)	500	500	300	300

Fig. 13 (a) Simulated temperature profile across a heater. Solid line: temperature profile during the heating cycle with a heating pulse magnitude of 7 V for a 30-μm heater. Dashed line: temperature profile during the cooling cycle. (b) Simulated cooling time (defined as the time needed for maximum heater temperature dropped below 50°C after the end of a heating cycle) versus heat barrier thickness. (c) Simulated liquid meniscus position for a 2-μm nozzle during chamber refill.

mental system. However, the predicted maximum operation frequency of our inkjet devices should be around 20 kHz, since the heating pulse width and the observed droplet formation time are all smaller than 5 μs, as discussed in the previous sections, while the system cooling time is around 15 μs according to our 1-D thermal diffusion simulation, and the simulated chamber refilling time is smaller than 5 μs. The simulation results are shown in Fig. 13. This frequency is close to the operational frequency of current inkjet cartridges and is hard to increase without sacrificing the droplet resolution. To achieve sufficient printing throughput with reduced pixel area, a larger, denser inkjet array could be used, which is feasible with our print head design and fabrication process. Since the area of each inkjet device can be smaller than 80×200 μm, a 100×100 inkjet array can be packed on a 1×2-cm^2 chip, almost the same area of a conventional inkjet cartridge. Using this print head and pattern resolution of 24000×12000 dpi, we could then process a page of A4 paper in 2 min, comparable to the speed of current inkjet printers.

6 Conclusion

We successfully develop a monolithic, ultra-high-resolution inkjet print head using silicon-based micromachining technology. The inkjet devices utilize a thermal bubble actuation mechanism and are designed to provide high actuation pressure and low flow resistance for small droplet generation. The print head is fabricated on a single silicon wafer with a large array of inkjet devices for high printing throughput. Each device is composed of a platinum heater stack, a fluid chamber formed by Ge sacrificial etching, a dry-etched micron-scale nozzle, and a fluidic channel opened by DRIE through-wafer etching. 3-μm water droplets have been reliably generated from this print head with uniform droplet size, velocity, and high trajectory precision. The resolution of inkjet printing systems could be improved almost four times using this print head. With good chemical compatibility, the print head is also capable of handling materials other than water, for micro/nano research areas, where delivery of small fluid droplets is required. Application of our inkjet print head to direct writing of micron-scale devices using solvent-based conducting, semiconducting, and insulating materials is presently under investigation.[27]

References

1. H. P. Le, "Progress and trends in ink-jet printing technology," *J. Imaging Sci. Technol.* **42**, 49–53 (1998).
2. E. Smouse, "Optimal design of desktop photo printing systems," *Imaging Sci. & Technol.*, pp. 91–95 (1998).
3. see http://www.epson.com/cgi-bin/Store/consumer/consDetail.jsp&BV_UseBVCookie=yes&infoType=Specs&oid=53540919&category=Products.
4. See http://www.usa.canon.com/consumer/controller&act=ModelDetailAct&fcategoryid=117&modelid=11993.
5. C. Kung, M. D. Barnes, N. Lermer, W. B. Whitten, and J. M. Ramsey, "Single-molecule analysis of ultradilute solutions with guided streams of 1 mu m water droplets," *Appl. Opt.* **38**(9), 1481–720 (1999).
6. P. W. Cooley, D. B. Wallace, and B. V. Antohe, "Application of ink-jet printing technology to BioMEMS and micro-fluidic systems," *Proc. SPIE* **4560**, 177–188 (2001).
7. H. Ago, K. Murata, M. Yumura, J. Yotani, and S. Uemura, "Ink-jet printing of nanoparticle catalyst for site-selective carbon nanotube growth," *Appl. Phys. Lett.* **82**, 811–813 (2003).
8. H. Sirringhaus, T. Kawaseetc., "High-resolution inkjet printing of all-polymer transistor circuits," *Science* **290**(5499), 2123–2126 (2000).
9. S. B. Fuller, E. J. Wilhelm, J. M. Jacobson, "Ink-jet printed nanoparticle microelectromechanical systems," *J. Microelectromech. Syst.* **11**(1), 54–60 (2002).
10. D. B. Bogy and F. E. Talke, "Experimental and theoretical study of wave propagation phenomena in drop-on-demand ink jet devices," *IBM J. Res. Dev.* **28**(3), 314–321 (1984).
11. F. C. Lee, "PZT printing applications, technologies, new devices," *Proc. Ultrasonic Symp.*, pp. 693–697 (1988).
12. S. Aden, J. Bohörquez, D. Collins, D. Crook, A. García, and U. Hess, "The third-generation HP thermal inkjet printhead," *Hewlett-Packard J.* **45**, 41–45 (1994).
13. P. A. Torpey, R. G. Markham, and Xerox Corporation, "Thermal inkjet print head," U.S. Pat. No. 4 638 337 (1987).
14. P. Krause, E. Obermeier, and W. Wehl, "Backshooter—a new smart micromachined single-chip inkjet printhead," *Tech. Dig. 8th Intl. Conf. Solid-State Sensors Actuators*, pp. 325–328 (1995).
15. J. Chen and K. D. Wise, "A high-resolution silicon monolithic nozzle array for inkjet printing," *IEEE Trans. Electron Devices* **44**(9), 1401–1409 (1997).
16. J. D. Lee, J. B. Yoon, J. K. Kim, H. J. Chung, C. S. Lee, H. D. Lee, H. J. Lee, C. K. Kim, and C. H. Han, "A thermal inkjet printhead with a monolithically fabricated nozzle plate and self-aligned ink feed hole," *J. Microelectromech. Syst.* **8**(3), 229–235 (1999).
17. F. G. Tseng, C. J. Kim, and C. M. Ho, "A high-resolution high-frequency monolithic top-shooting microinjector free of satellite drops," *J. Microelectromech. Syst.* **11**, 427–447 (2002).
18. S. S. Baek et al., "A novel back-shooting inkjet printhead using trench-filling and SOI wafer," *Sens. Actuators, A* **114**, 392–397 (2004).
19. D. Huang and E. S. Kim, "Micromachined acoustic wave liquid ejector," *J. Microelectromech. Syst.* **10**, 442–449 (2001).
20. S. Kamisuki, T. Hagata, C. Tezuka, Y. Nose, M. Fujii, and M. Atobe, "A low power, small, electrostatically-driven commercial inkjet head," *Proc. IEEE Micro Electro Mechanical Syst.*, pp. 63–68 (1998).
21. R. R. Allen, J. D. Meyer, and W. R. Knight, "Thermodynamics and hydrodynamics of thermal ink jets," *Hewlett-Packard J.* **36**, 21–27 (1985).
22. See http://www.coventor.com/coventorware/inkjet/.
23. A. Asai, "Bubble dynamics in boiling under high heat flux pulse heating," *ASME Trans. J. Heat Transfer* **113**(4), 973–979 (1991).
24. A. Asai, "Three-dimensional calculation of bubble growth and drop ejection in a bubble jet printer," *ASME Trans. J. Fluids Eng.* **114**(4), 638–641 (1992).
25. J. D. Beasley, "Model for fluid ejection and refill in an impulse drive jet," *Photograph. Sci. Eng.* **21**(2), 78–82 (1977).
26. V. Eldurkar and J. S. Aden, "Development of the thin-film structure for the thinkjet printhead," *Hewlett-Packard J.* **36**, 27–33 (1985).
27. Y. Wang, J. Bokor, and A. Lee, "Maskless lithography using drop-on-demand inkjet printing method," *Proc. SPIE* **5374**, 628–636 (2004).
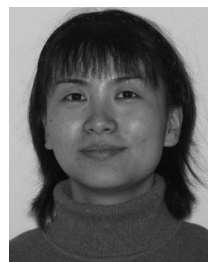
Yan Wang received the BS degree in physics from Beijing University, China, in 1997, and PhD degree in field of electrical engineering from the University of California at Berkley in 2005. Her PhD project focused on developing a maskless lithography system using the drop-on-demand inkjet printing method. She has been working as a senior process device engineer in the technology department of Xilinx Incorporated since 2004. Her job duties include building optical lithography models and developing design for manufacturing (DFM) systems for Xilinx's most advanced FPGA products.

Jeffrey Bokor received the BS degree in electrical engineering from the Massachusetts Institute of Technology in 1975, and the MS and PhD degrees in electrical engineering from Stanford University in 1976 and 1980, respectively. From 1980 to 1993, he was at AT&T Bell Laboratories, where he did research on novel sources of ultraviolet and soft x-ray coherent radiation, advanced lithography, picosecond optoelectronics, semiconductor physics, surface physics, MOS device physics, and integrated circuit process technology. He held management positions as head of the laser science research department at Bell Labs in Holmdel, New Jersey, from 1987 to 1990, and head of the ULSI technology research department at Bell Labs in Murray Hill, New Jersey, from 1990 to 1993. He was appointed professor of electrical engineering and computer sciences at the University of California at Berkeley in 1993, with a joint appointment at the Lawrence Berkeley National Laboratory (LBNL). In 2004, he was appointed as deputy director for the Science at the Molecular Foundry at LBNL, a major new nanoscale science research center. His current research activities include novel techniques for nanofabrication, new devices for nanoelectronics, quantum information processing, extreme ultraviolet lithography, optical metrology, and Fourier optics. He is a fellow of IEEE, APS, and OSA.